

Predicting X-ray emission from wind-blown bubbles – Limitations of fits to *ROSAT* spectra

David K. Strickland and Ian R. Stevens

School of Physics and Astronomy, The University of Birmingham, Edgbaston, Birmingham, U.K. B15 2TT
dks@star.sr.bham.ac.uk, irs@star.sr.bham.ac.uk

Accepted; Received; in original form

ABSTRACT

Wind-blown bubbles, from those around massive O and Wolf-Rayet stars, to superbubbles around OB associations and galactic winds in starburst galaxies, have a dominant role in determining the structure of the Interstellar Medium. X-ray observations of these bubbles are particularly important as most of their volume is taken up with hot gas, $10^5 \lesssim T(\text{K}) \lesssim 10^8$.

However, it is difficult to compare these X-ray observations, usually analysed in terms of single or two temperature spectral model fits, with theoretical models, as real bubbles do not have such simple temperature distributions. Spectral fits, and the properties inferred from them, will depend in a complex way on the true temperature distribution and the characteristics and limitations of the X-ray observatory used.

In this introduction to a series of papers detailing the *observable* X-ray properties of wind-blown bubbles, we describe our method with which we aim to solve this problem, analysing a simulation of a wind-blown bubble around a massive star.

Our model is of a wind of constant mass and energy injection rate, blowing into a uniform ISM, from which we calculate X-ray spectra as would be seen by the *ROSAT* PSPC. Analysing these spectra in the same way as a real observation would be, we compare the properties of the bubble as would be inferred from the *ROSAT* data with the true properties of the bubble in the simulation.

We find standard spectral models yield inferred properties that deviate significantly from the true properties, even though the spectral fits are statistically acceptable, and give no indication that they do not represent to true spectral distribution. For example, single temperature spectral fits give best fit metal abundances only 4% of the true value. A cool bubble has best fit temperatures significantly higher than a bubble twice as hot. These results suggest that in any case where the true source spectrum does not come from a simple single or two temperature distribution the “observed” properties cannot naively be used to infer the true properties. In this situation, to compare X-ray observations with theory it is necessary to calculate the *observable* X-ray properties of the model.

Key words: Methods: data analysis – Methods: numerical – ISM: bubbles – X-rays: interstellar

1 INTRODUCTION

Bubbles blown in the Interstellar Medium (ISM) by massive stars are a common astrophysical phenomenon. X-ray observations can provide information regarding the density, metal abundance, temperature, ionisation state and physical structure in the hot bubbles surrounding Wolf-Rayet (WR) and O stars (Wrigge, Wendker & Wisotski 1994), Luminous Blue Variables (LBV’s) such as η Carinae (Corcoran et al. 1995) and planetary nebulae (PN) (Kreysing et al. 1992; Leahy, Zhang & Kwok 1994; Arnaud, Borkowski

& Harrington 1996; Leahy et al. 1996). On the larger scale, superbubbles are created by the sum of the winds and SN within OB associations (Belloni & Mereghetti 1994) and giant star forming regions in young starburst galaxies. Superbubbles within starburst galaxies such as M82 eventually break out the galaxy to form spectacular galactic winds (Watson, Stanger & Griffiths 1984; Heckman, Armus & Miley 1987). In many cases the X-ray emission probes different regions of the object in question to that revealed by optical observations, increasing the importance of the X-ray data.

Analytic solutions to the development and structure of

astrophysical bubbles must rely on simplifying assumptions, and increasingly attention has turned to the use of numerical hydrodynamics. These simulations have been enlightening with respect to the nonlinear processes occurring, with some degree of quantitative agreement with observation, but generally lack predictive power. This is partially due to the difficulty in comparing them with observations, in particular X-ray observations.

The problem is that X-ray observations are usually analysed by fitting a single or two temperature spectral model to the observed spectra (see for example the references above), and the best-fit results are used to infer the physical properties of the object.

However, for wind-blown bubbles such as those mentioned above, the true situation is more complex, and the results of the spectral fits may be influenced by, for example: projection of different physical regions along the line of sight; the presence of a wide range of temperatures; interstellar absorption; unknown or non-standard elemental abundances; non-ionisation equilibrium conditions; low numbers of observed photons and the limitations of the current X-ray telescope optics and detectors.

All of these make the interpretation of what is normally a one or two temperature spectral fit to the data difficult to relate to the underlying physical conditions, and conversely, make it difficult to predict the *observable* properties of a model or simulation.

To our knowledge there has been no study of the influence of the complexities mentioned above on the best-fit properties of a spectral fit to the observable X-ray data, and in particular not for wind blown bubbles. As we shall show, the combination of the physical effects above and the properties (and limitations) of real X-ray observatories, can significantly affect the results of simple spectral fitting.

Previous authors (Weaver et al. 1977; Zhekov & Perinotto 1996) have calculated theoretical X-ray spectra from their 1-D models, but did not consider particular instruments or fit models to those spectra. In general only X-ray luminosities are calculated (*e.g.* Volk & Kwok 1985; Mellema & Frank 1995; Garcia-Segura & Mac Low 1995).

The aim of this paper is to introduce a method of analysing numerical simulations in the same way as actual X-ray observations are analysed, *i.e.* predict the *observable* X-ray properties. This method can be applied to a wide range of phenomenon where X-rays are important, from wind-blown bubbles around WR stars and PN, through the larger bubbles around clusters of massive stars to starburst-driven galactic winds.

We simulate a wind blown bubble using a 2-dimensional hydrodynamic code, concentrating on the properties of the hot X-ray emitting gas. The hydrodynamic model is used to generate artificial X-ray spectra and images, in particular simulated *ROSAT* spectra. We then analyse these spectra in the same way as real *ROSAT* spectra would be, in order to determine what the observationally determined properties of the bubble would be, and how those relate to its actual structure. This synthesis is necessary to a) determine the physical processes that are observationally important, and b) *allow a direct comparison between observation and theory.*

Our model of a wind-blown bubble is deliberately chosen to be the simplest applicable model with an analytic solution, in order to simplify the analysis of our results, and

avoiding added complications that a more physically accurate model of a wind blown bubble (*e.g.* Garcia-Segura, Mac Low & Langer 1996) would introduce into the interpretation of our results. Later papers will consider more realistic models, with additional physics such as time varying energy and mass injection rates, along with spatial variation of the X-ray properties. This will be necessary to understand the properties of the extended emission from galactic winds (see for example Strickland, Stevens and Ponman 1997).

In Section 2 we describe the numerical code used to produce the results shown in Section 3. Section 4 discusses the implications of these results, and we briefly sum up in Section 5.

2 NUMERICAL METHOD

The 2-D numerical simulations presented in this paper were performed using VIRGINIA HYDRODYNAMICS-1 (VH-1), written by John Blondin and co-workers (Blondin et al. 1990). VH-1 is based on the piecewise parabolic method (PPM) of Colella & Woodward (1984), which is a third order accurate finite difference algorithm. For a more detailed description of the code see Stevens, Blondin & Pollock (1992).

Radiative cooling is handled assuming optically thin gas with solar abundance ratios and ionisation equilibrium. The cooling curve for the temperature range $4.0 \leq \log T \leq 8.6$ was generated using the Raymond-Smith plasma code (Raymond & Smith 1977), assuming solar element abundances. Because cooling times at $T \sim 10^5$ K are short, we place a limit of the numerical timestep to prevent more than a 2% energy loss per computational cell per timestep. For $T \leq 10^4$ K the cooling is set to zero.

For the simulations described below VH-1 was run in cylindrical coordinates (r, z) , assuming symmetry around the z -axis. In practice this gives rise to numerical artifacts along the coordinate axes, but these are small and do not affect our results. The computational grid consisted of 400×400 cells of equal size, spanning a physical distance of $r_{\max} = z_{\max} = 2.0 \times 10^{19}$ cm.

2.1 Simple wind-blown bubble model

As a simple realistic model of a wind-blown bubble we consider the analytical model of Castor, McCray & Weaver (1975) and Weaver et al. (1977). A wind of constant terminal velocity v_W and mechanical luminosity $L_W = \frac{1}{2} \dot{M}_W v_W^2$ (where \dot{M}_W is the mass loss rate of the star) blows into a medium of uniform density ρ_0 . This generates a bubble with a structure divided into three distinct regions: an outer shock, separating the undisturbed ambient ISM from a shell of swept up and shocked ISM; a bubble of hot shocked stellar wind material, bounded at its outer edge by a contact discontinuity between it and the shell of shocked ISM, and at its inner edge by a reverse shock between it and the third innermost region of the freely expanding stellar wind. After several thousand years the shell of swept up ISM cools and collapses down to form denser, cold ($T \sim 10^4$ K) shell, which is the source of the the optical emission associated with the nebula.

In the standard Weaver et al. (1977) model thermal conduction leads to evaporation of matter off the dense shell of

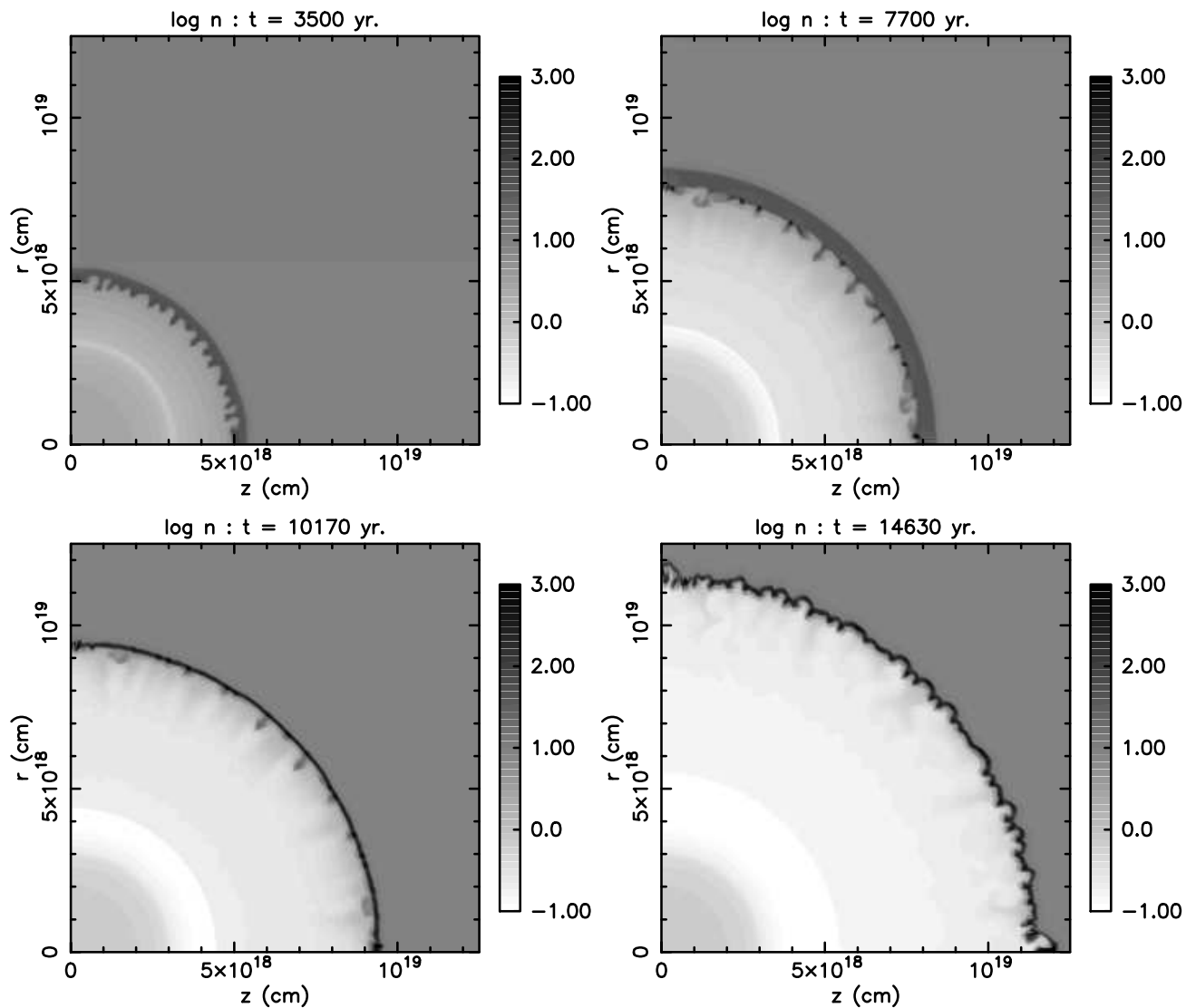


Figure 1. Logarithm of the gas number density during the simulation at $t = 3500$, 7700 , 10170 and 14630 yr. At $t = 3500$ yr the bubble has suffered no significant radiative energy loss. Shell collapse is underway at 7700 yr, approximately the time of maximum soft X-ray luminosity, and has just finished at 10170 yr. The bubble then enters the self-similar phase, its properties at $t = 14630$ yr being typical of this stage.

swept-up ISM into the hot bubble interior, cooling it and significantly increasing its density. In common with many of the hydrodynamical simulations of bubbles we do not include conduction. Magnetic fields may suppress conduction, even at very low B-field strengths that otherwise are dynamically unimportant (Soker 1994; Band & Liang 1988). Given the limited observational knowledge on the state of magnetic fields and conduction within bubbles we choose to ignore both!

We shall consider two simulations, both with $L_W = 6.3 \times 10^{37} \text{ erg s}^{-1}$. To obtain different temperatures in the hot bubble we vary the wind mass loss rate between simulations. The low mass loss rate simulation has $\dot{M}_W = 5 \times 10^{-5} M_\odot \text{ yr}^{-1}$. In the high mass loss rate simulation

$\dot{M}_W = 1 \times 10^{-4} M_\odot \text{ yr}^{-1}$, giving a bubble of half the temperature of the low mass loss rate simulation. Mass and energy are added to cells within $r = 3 \times 10^{18}$ cm at each timestep. The ambient medium is assumed to be uniform and totally ionised, with a total number density of $n_0 = 10 \text{ cm}^{-3}$.

2.2 Simulated X-ray data

We shall only consider simulated *ROSAT* PSPC (Position Sensitive Proportional Counter) data. Although the gas proportional counter's spectral resolution of $\Delta E/E \approx 0.43(E/0.93)^{-0.5}$ (FWHM, with E measured in keV) is low compared to a mission such as *ASCA*, wind-blown bubbles

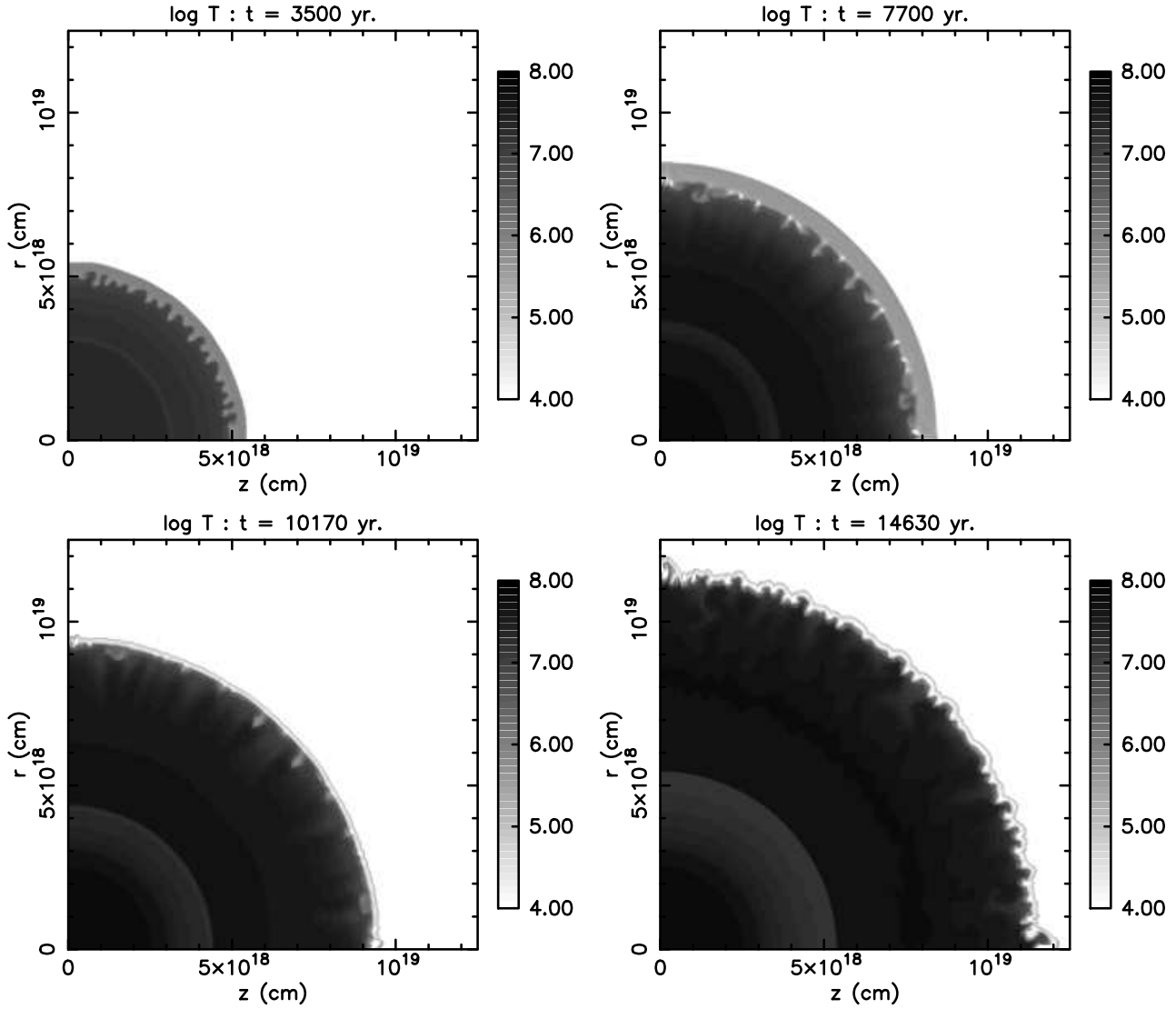


Figure 2. As Fig. 1 but greyscales of $\log_{10} T$ (K).

Table 1. Model parameters for the two bubble simulations

| Parameter | Value |
|---------------------------|--|
| Wind luminosity L_W | $6.3 \times 10^{37} \text{ erg s}^{-1}$ |
| Mass loss rate M_W | 5×10^{-5} or $1 \times 10^{-4} M_\odot \text{ yr}^{-1}$ |
| Wind velocity v_W | 2000 or 1414 km s^{-1} |
| ISM ambient density n_0 | 10 cm^{-3} |
| Distance to bubble | 2 kpc |
| Absorbing column N_H | $3.16 \times 10^{21} \text{ cm}^{-2}$ |
| Grid size | $2 \cdot 10^{19} \text{ cm} \times 2 \cdot 10^{19} \text{ cm}$ |
| Cell size | $5 \cdot 10^{16} \text{ cm} \times 5 \cdot 10^{16} \text{ cm}$ |

are soft X-ray sources and *ROSAT* has more sensitivity than *ASCA* at low energies.

For a detailed discussion of the *ROSAT* satellite see ‘The *ROSAT* user’s handbook’ (Briel et al. 1994).

3 RESULTS

As the low and high mass loss rate simulations only differ in the density and temperature of the shocked wind, we shall concentrate on describing the low mass loss rate simulation below. Section 3.4 describes how the results of the high mass loss rate bubble differ from those given below.

3.1 Bubble growth

There are three definable stages of bubble growth seen in the simulation. These are i) before the shell cools, ii) during shell cooling and collapse, and iii) self-similar growth after shell collapse with a thin cold ($T \sim 10^4$ K) shell. The 1-dimensional analytic solutions for the first and last of these stages are presented in detail in Castor et al. (1975) and Weaver et al. (1977).

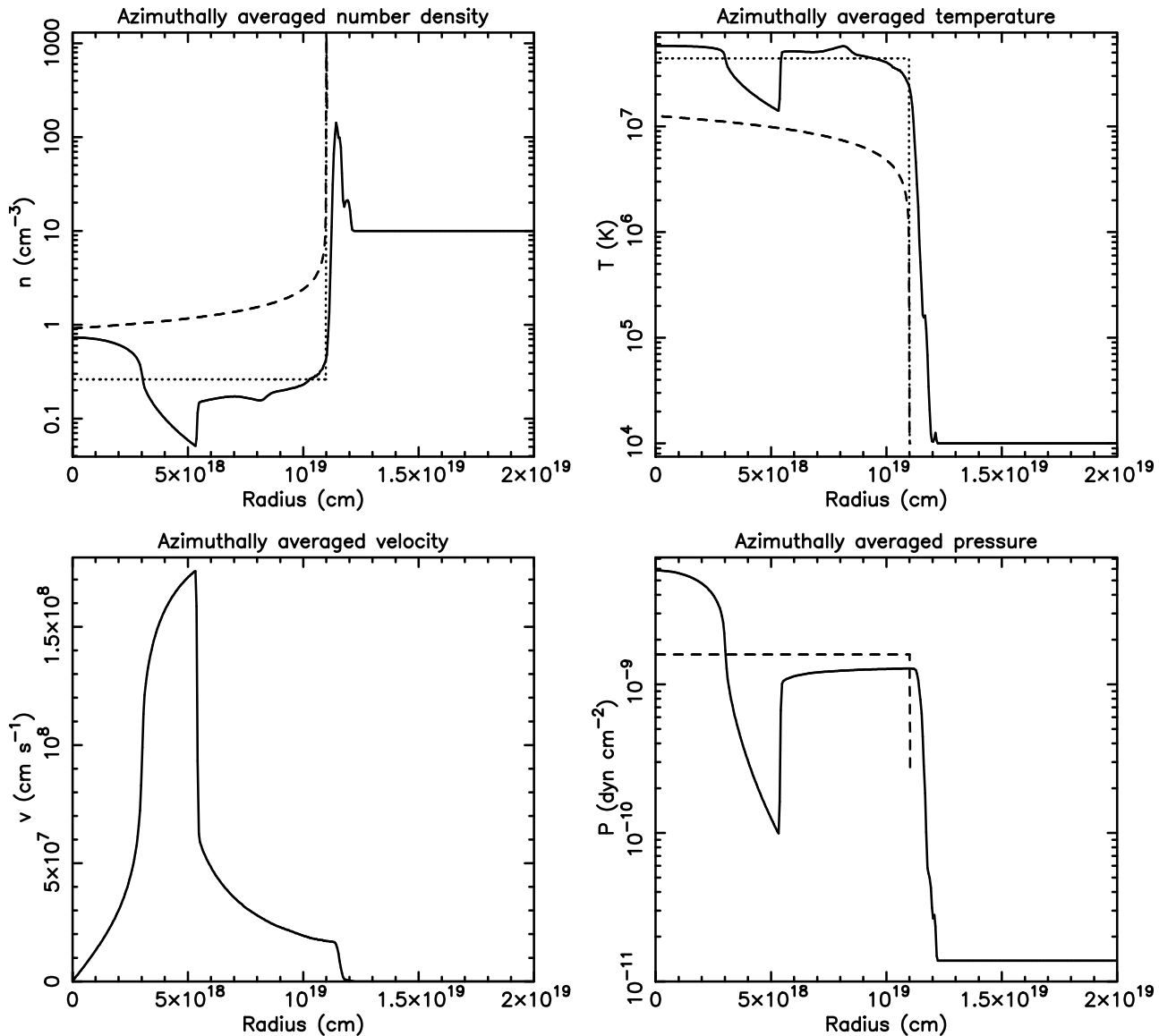


Figure 4. Radial profiles of density, temperature, velocity and pressure (solid lines) from the low mass loss rate simulation, compared to the predictions from the Weaver et al. (1977) model (with conduction: dashed line, no conduction: dotted line), at $t = 14630$ yr. Note that the Weaver model only applies for $R > R_1$, the radius of the wind termination shock.

Initially the swept up ISM is shock-heated to $5.5 \lesssim \log T(\text{K}) \lesssim 6.0$. The shell is thick (see Figs. 1 and 2), and a strong emitter of extreme Ultraviolet (EUV) radiation and soft X-rays, as can be seen from the 0.1-2.4 keV luminosity (Fig. 3). The major coolant is radiation in the UV-EUV rather than X-rays, the UV-EUV luminosity being of order a magnitude greater than the soft X-ray luminosity before shell collapse. The luminosity rises rapidly with time, as the bubble sweeps up and heats more ISM. The rate of increase of luminosity decreases after $t \approx 4000$ yr, the X-ray luminosity peaking at $L_X = 1.9 \times 10^{36} \text{ erg s}^{-1}$ at $t \approx 6300$ yr as the shell begins to cool. The UV-EUV luminosity peaks later, at ≈ 8100 yr as the shell cools further out of the X-ray band and becomes denser. The peak UV-EUV luminosity of $9.1 \times 10^{37} \text{ erg s}^{-1}$ briefly exceeds the wind energy input. Af-

ter shell collapse X-ray luminosities are approximately two orders of magnitude below the UV-EUV luminosity, both remaining essentially constant for the duration of the simulation.

Following shell collapse shell densities are typically several hundred to a few thousand particles per cubic centimetre, with $T \approx 10^4$ K.

In the absence of heat conduction and evaporation off the cool shell, we would simplistically expect the bubble interior to have a uniform low density and high temperature. In this case the shocked-wind material has the same pressure as predicted by Castor et al. (1975) and Weaver et al. (1977), but the temperature determined by the reverse shock (the termination shock of the freely expanding wind).

In practice, the density rises in as the shell is ap-

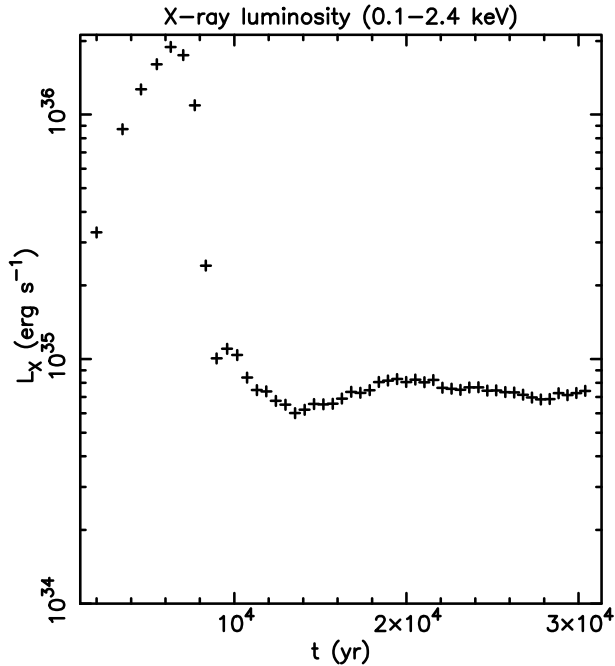


Figure 3. Bubble X-ray luminosity as a function of time in the *ROSAT* 0.1–2.4 keV band.

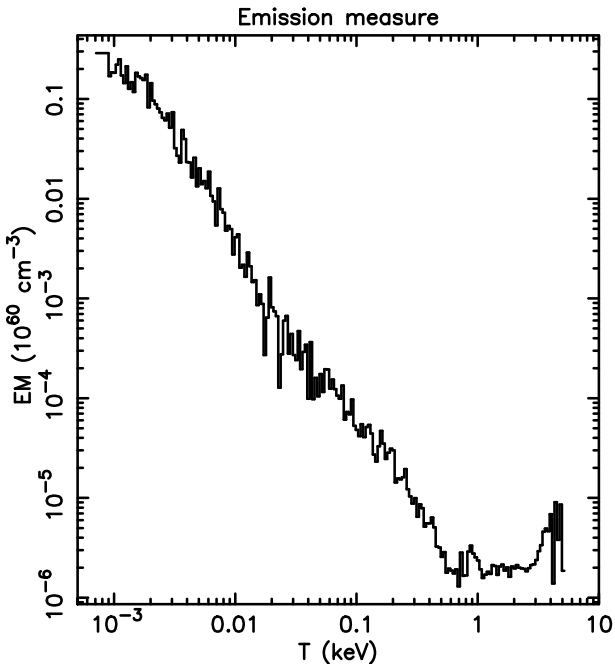


Figure 5. The emission measure as a function of temperature ($EM_T = \int n_e^2 \times dV_T$) for the entire bubble at $t = 15000$ yr.

proached, and the temperature drops, although not to the extent expected for true conduction. This can be seen in both the 2D images of Figs. 1–2 and the radial profiles of Fig. 4. This is due to eddies and swirling motions along the shell–bubble interface mixing material from the dense shell into the hot bubble interior. The outward velocity in the shocked-wind is higher than the velocity at which the shell expands into the ISM (Fig. 4), and coupled with the corru-

gations seen on the inside surface of the shell, shear motions arise between the faster bubble interior and the shell, leading to swirling motions along the interface and the introduction of cooler, denser material into the hot bubble.

In a perfectly spherically symmetric bubble, the lack of a tangential velocity component between the faster-expanding bubble interior and the shell would prevent such stripping of material off the shell. In our simulations, the bubble–shell interface is corrugated by instabilities from early on in the simulation, presenting faces not totally perpendicular to the flow in the bubble interior, and leading to mixing.

3.1.1 Shell instabilities

The instabilities of the shell seen in Figs. 1 and 2 have important consequences as they lead to the introduction of cooler, denser material into the bubble interior, hence modifying the X-ray emitting properties of the bubble.

The shell should be stable against Rayleigh–Taylor instabilities, as it is constantly decelerating, suggesting that the instabilities are Vishniac instabilities (Vishniac 1983).

The initial seed perturbation is numerical artifact, arising when the forward shock first appears at the start of the simulation, and is due to the orthogonal nature of the computational grid and the finite size of the energy injection region.

Does this instability, and the cooler material it injects into the hot shocked wind region, render the results of these simulations untenable? In real system such as wind-blown bubbles around individual stars or superbubbles, both the wind energy injection rate and the ISM will be far from uniform, so instabilities and inhomogeneities in the shell are to be expected. Note that conduction would introduce far more cool material into the bubble interior than these instabilities do (Fig. 4). Mass loading of the flow by ablation of clumps and cloudlets (*c.f.* Hartquist et al. 1986) will also add cool dense material. We are therefore not worried that our 2D simulations do not exactly match the 1D analytic prediction, as the mass introduced into the bubble interior is by no means unphysically large.

3.2 Bubble structure and properties at $t = 15000$ yr

For a more detailed study of the observable X-ray properties we shall investigate the bubble at $t = 14630$ yr (hereafter 15000 yr for convenience). The bubble at this time has settled down into self-similar expansion with a thin shell, the period described by the standard solution of Castor et al. (1975) and Weaver et al. (1977).

3.2.1 Comparison with the Weaver et al. model

The properties of our simulated bubble at $t = 15000$ yr and the predictions of the Weaver et al. (1977) for the same input parameters are encouragingly similar, if we modify the standard Weaver et al. model to account for the *lack* of thermal conduction in the VH-1 code (Fig. 4 and Tables 2 and 3).

To illustrate the effect that conduction would have on

Table 2. Bubble properties at $t = 15000$ yr. The X-ray fluxes in the *ROSAT* 0.1–2.4 keV band and *ROSAT* PSPC count rates are given for zero column (intrinsic) and $N_{\text{H}} = 3.16 \times 10^{21} \text{ cm}^{-2}$ (absorbed).

| Parameter | Value |
|----------------------------|---|
| Reverse shock radius R_1 | $5.3 \times 10^{18} \text{ cm}$ |
| Forward shock radius R_2 | $1.17 \times 10^{19} \text{ cm}$ |
| Total energy radiated | $1.057 \times 10^{49} \text{ erg}$ |
| Thermal energy | $1.169 \times 10^{49} \text{ erg}$ |
| Kinetic energy | $6.824 \times 10^{48} \text{ erg}$ |
| Shell velocity | $126\text{--}166 \text{ km s}^{-1}$ |
| Total volume | $6.702 \times 10^{57} \text{ cm}^3$ |
| Total mass | $34.4 M_{\odot}$ |
| Total emission measure | $4.409 \times 10^{60} \text{ cm}^{-3}$ |
| Luminosity (0.1–2.4 keV) | $6.55 \times 10^{34} \text{ erg s}^{-1}$ |
| f_X (int.) | $1.36 \times 10^{-10} \text{ erg s}^{-1} \text{ cm}^{-2}$ |
| PSPC count rate | $35.3 \text{ photons s}^{-1}$ |
| f_X (abs.) | $3.54 \times 10^{-12} \text{ erg s}^{-1} \text{ cm}^{-2}$ |
| PSPC count rate | $0.3156 \text{ photons s}^{-1}$ |

Table 3. Bubble properties at $t = 15000$ yr as predicted by the Weaver et al. (1977) model.

| Parameter | Value |
|---------------------------------------|--|
| Reverse shock radius R_1 | $4.2 \times 10^{18} \text{ cm}$ |
| Forward shock radius R_2 | $1.1 \times 10^{19} \text{ cm}$ |
| Thermal energy in shocked wind | $1.32 \times 10^{49} \text{ erg}$ |
| Kinetic energy in shell | $5.67 \times 10^{48} \text{ erg}$ |
| Shell velocity | 143 km s^{-1} |
| Total volume (including shell) | $5.6 \times 10^{57} \text{ cm}^3$ |
| Total mass (including shell) | $28.7 M_{\odot}$ |
| Luminosity ^a (0.1–2.4 keV) | $2.39 \times 10^{35} \text{ erg s}^{-1}$ |
| Luminosity ^b (0.1–2.4 keV) | $8.94 \times 10^{32} \text{ erg s}^{-1}$ |

^a Including thermal conduction.

^b Without conduction.

the structure of the bubble, the properties of the standard Weaver et al. bubble with conduction (with thermal conductivity of the form $K(T) = CT^{5/2}$, where $C = 1.2 \times 10^{-6} \text{ erg s}^{-1} \text{ cm}^{-1} \text{ K}^{-7/2}$ (Spitzer 1962)) are also given in Fig. 4 and Table 3.

Note that the analytical predictions only apply for $R \geq R_1$, the radius of the reverse shock, although they are shown in Fig. 4 extending all the way to the center of the bubble. In Castor et al. (1975) and Weaver (1977) the free-wind region inside R_1 is ignored, which as we shall discuss below, does lead to minor differences between simulation and theory.

Due to the way we have injected mass and energy onto the computational grid, the region inside R_1 corresponds to the solution of Chevalier and Clegg (1985), rather than a point-like source of mass and energy.

The Weaver et al. model’s shell is much thinner than the *azimuthally averaged* profile from the simulation, as the shell is corrugated and hence spread out over radius. Inspecting the 2-D data the peak densities in the simulations agree well with the density predicted by the analytical model, implying that the dense shell is not significantly unresolved. The bubble in the simulation is slightly larger than predicted, but this is not surprising as this reflects the “head-start” we have given the simulated bubble by injecting mass and energy over a finite input region.

Densities (temperatures) in the shocked-wind rise (drop) near the shell, compared to the analytic prediction,

due to the mixing of cooler material into the bubble as discussed in Section. 3.1.1. This increases the bubble X-ray luminosity from $L_X = 8.94 \times 10^{32} \text{ erg s}^{-1}$ in Table. 3 for a non-conductive bubble to an appreciable $6.55 \times 10^{34} \text{ erg s}^{-1}$, only a factor ~ 3 less than for a bubble with thermal conduction.

The thermal pressure in the shocked wind in our simulation is less than that predicted by the Weaver et al. model. In the analytic solution it is assumed that the energy contained in the free-wind region is negligible, and that all the energy in the shocked wind is thermal. In practice this is not the case, although the majority of the energy is thermal energy in the shocked wind. The velocities in the shocked wind are appreciable (see Fig.4). Coupled with the appreciable energy loss that accompanied shell collapse this leads to lower than expected thermal energy in the shocked wind, and hence lower pressure.

3.2.2 Simulated ROSAT spectra

We generate and fit theoretical X-ray spectra by the following process. The 2-Dimensional density and temperature data from VH-1 are rotated around the axis of symmetry to produce a temporary 3-D dataset. The MEKAL (Mewe, Kaastra & Liedahl 1995) plasma code is used to calculate the X-ray emission from each volume of gas, assuming ionisation equilibrium and solar element abundances. It is also assumed the gas is optically thin to its own radiation, and that any absorption the X-rays suffer is extrinsic to the source. External absorption is modeled as a uniform foreground screen, using the coefficients given in Morrison & McCammon (1983).

The raw high resolution X-ray spectrum generated by the plasma code (see Fig. 6) is corrected for a typical absorbing column of $3.16 \times 10^{21} \text{ cm}^{-2}$, appropriate for the wind-blown bubble NGC 6888 (Wrigge, Wendker & Wisotzki 1994), and then folded through the spectral response of the *ROSAT* PSPC, assuming a source distance of 2 kpc for the bubble.

No X-ray background is included, effectively assuming a perfect background subtraction. We estimate that the soft X-ray background would have a PSPC count rate of ≈ 0.19 counts s^{-1} over the area of sky occupied by the bubble at $t = 15000$ yr, based on the *ROSAT* PSPC observation of M82 (Strickland et al. 1997). The detector count rate due to the bubble itself is 0.32 counts s^{-1} for an absorbing column of $3.16 \times 10^{21} \text{ cm}^{-2}$.

Note that the time to reach ionisation equilibrium, $t_{\text{ieq}} \approx 10^{12} n_e^{-1} \text{ s}$ (*c.f.* Masai 1994) is greater than the bubble’s age over much of the volume. As our aim is to see whether fits to *ROSAT* spectra can accurately reflect the true bubble properties, the assumption of ionisation equilibrium is not a problem.

3.2.3 A simple estimator of the fitted temperature.

Are there easier ways of predicting the observable properties of a model than generating and fitting artificial X-ray spectra? This method is also instrument specific, as it depends on the spectral characteristics of the instrument used, and so predicted results for *ROSAT* are not directly transferable to, *e.g.* *ASCA*.

If we *assume* we can correctly estimate the absorbing column and metallicity, either from a spectral fit or from observations at other wavelengths, then estimating a characteristic temperature is all we need do.

We might expect the fitted temperature to be some flux-weighted average of the true temperature range, and the emission measure roughly the total emission over the range of temperatures *ROSAT* is sensitive to.

Over the energy range 0.005-15.0 keV the intrinsic flux (*i.e.* unabsorbed) weighted average temperature $\langle T_{EW} \rangle = (4.9_{-1.3}^{+2.7}) \times 10^{-3}$ keV, *i.e.* UV emission from very cool material at the shell-bubble interior interface. In practice all the mid and extreme UV emission is absorbed in the intervening ISM. In addition the instrument response further limits the “observed” temperature.

If we assume that we can accurately remove the effects of interstellar absorption on the X-rays (*i.e.* fitting the column correctly) then to construct a predicted *ROSAT* temperature we need only weight each temperature by the count rate in the *ROSAT* PSPC due to each temperature component, ignoring absorption. This temperature is $\langle T_{ROSAT} \rangle = 0.0988_{-0.046}^{+0.268}$ keV. Given the true temperature distribution in Fig. 5 the *ROSAT* emission-weighted average temperature is more a reflection of the instrument response than a fair estimation of the temperature of the emitted radiation or the general state of the bubble.

$\langle T_{ROSAT} \rangle$ is instrument specific, defeating our object of trying to produce an instrument-independent estimator for the temperature. This may well be impossible, in such a situation as this where the temperature distribution can not be described by a single, characteristic temperature.

The emission measure should follow from the normalisation of the spectrum. and will depend on the best-fit values for the other parameters which determine the shape of the model spectrum. For the purposes of comparison between the results of the spectral fitting below and the “true” values, the total emission measure between $0.01 \leq T(\text{keV}) \leq 10.0$ is $3.77 \times 10^{58} \text{ cm}^{-3}$. Between $0.1 \leq T(\text{keV}) \leq 2.4$, it is $8.64 \times 10^{56} \text{ cm}^{-3}$.

3.2.4 Spectral fitting

For an assumed exposure time of 3000s we obtain a simulated *ROSAT* PSPC spectrum containing ~ 1000 counts. To assess the effect of real photon statistics, and the consequent variation in best-fit parameters, on our simulated spectra we generated ten Poisson realizations, fitting each using the STARLINK X-ray analysis package ASTERIX. The number of counts per bin is sufficient to allow the use of χ^2 fitting.

Three different spectral models were considered: a standard single temperature absorbed hot plasma model; a two temperature model, with both components having the same absorbing column and metal abundance, and finally a differential emission measure model.

Single temperature models are widely used to characterise X-ray emission, and it is only when there are sufficient counts to show that a single temperature model is a bad fit that more complex models are used. It is therefore sensible to fit such a model, despite knowing that the true temperature distribution of the X-ray emitting plasma is far from being single temperature (see Fig. 5).

A two temperature model would be the next level of complexity, naively a soft component for cooler denser gas near the shell and a hot component for the bubble interior.

The differential emission model attempts to incorporate the emission of gas at a wider range of temperatures by specifying the emission measure $EM = \int n_e^2 dV$ is a power law in temperature, *i.e.* $EM \propto T^\gamma$, between two temperatures T_{low} and T_{high} .

We quote results for models with all parameters fitted for (including the column and the metallicity) and for fits with the metallicity fixed at solar abundance. Although in practice we know the absorbing column applied, fits with it fixed were statistically unacceptable. For the purpose of display and interpretation, the best-fit results for each of the ten Poisson realisations were averaged. The quoted errors are the statistical deviations of the best-fit results, and not the fitted confidence regions. Typically, the 68% confidence regions (for one parameter of interest) were smaller or of order the deviations quoted.

The results for the fits to the integrated bubble spectrum are given in Tables. 4, 5 and 6.

The best fit models look very similar when convolved with PSPC instrument response (*i.e.* as they are when compared with the data), despite the very different fit parameters (Fig. 7). The only noticeable differences are the width of the peak at channels equivalent to $E \sim 0.8$ keV, and how the model fits to points between $1.5 \lesssim E(\text{keV}) \lesssim 2.0$.

The reason the single temperature, metallicity fixed at solar, spectral fits are bad is that they fail to fit these higher energy points at all. Freeing the metallicity to fit allows the shape of the spectrum to be changed. the temperature increases to better fit the higher energy points, and the metallicity drops to change the relative shape of the spectrum around the Iron-L complex (effectively the only lines *ROSAT* spectral fitting is sensitive too). Similarly the absorption column changes the shape of the spectrum. In the fits with metallicity free to fit, the increased temperature move the spectrum towards higher energies, removing the requirement to absorb as much low energy flux, hence low best fit columns.

The two temperature and differential emission measure models give better fits, as the hot component (or hot components in the case of the differential emission measure model) fit the high energy points present in the spectrum, freeing the cool component to fit at a lower temperature. The available trade-off between the various components in these multi-component models make the best-fit parameter less constrained, and insensitive to the metal abundance.

We shall defer further interpretation and discussion of these results, and what they would lead us to infer about the bubble’s properties, to Section. 4.1.5.

3.3 Spectral variation over time

The spectral properties of the bubble after shell collapse will be different to those prior to shell cooling. At early times, as discussed above, the shell is the major source of X-rays, and dominates the emission. It is only after the shell cools from its initial temperature of $T \sim 10^6$ K to the final temperature of $T \sim 10^4$ K that the X-ray emission from the bubble interior, *i.e.* the shocked wind itself, becomes significant.

This is graphically illustrated by Figs. 8 and 9. Note how

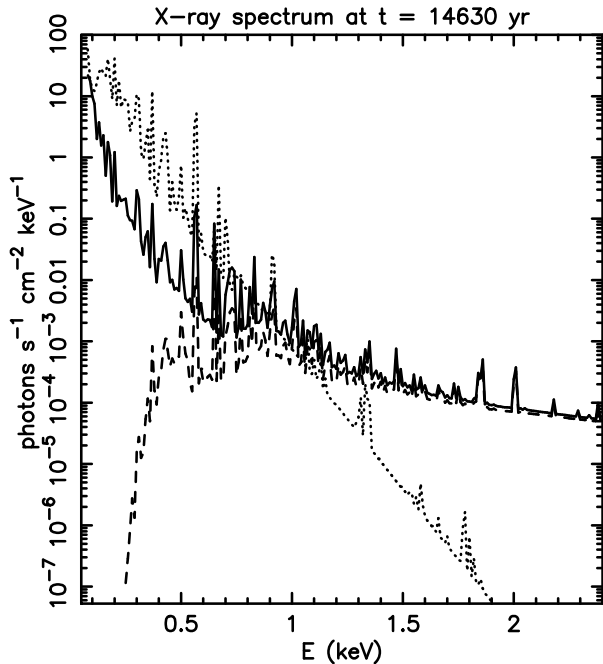


Figure 6. X-ray spectra for the bubble at $t = 15000$ yr, unconvolved with any instrument response. The solid and dashed lines correspond to absorbing columns of $N_{\text{H}} = 0.0$ and $3.16 \times 10^{21} \text{ cm}^{-2}$ respectively. For comparison an unabsorbed $T = 0.1$ keV spectrum of arbitrary normalisation is shown dotted. Note that despite being soft the bubble's spectrum does have a hard tail.

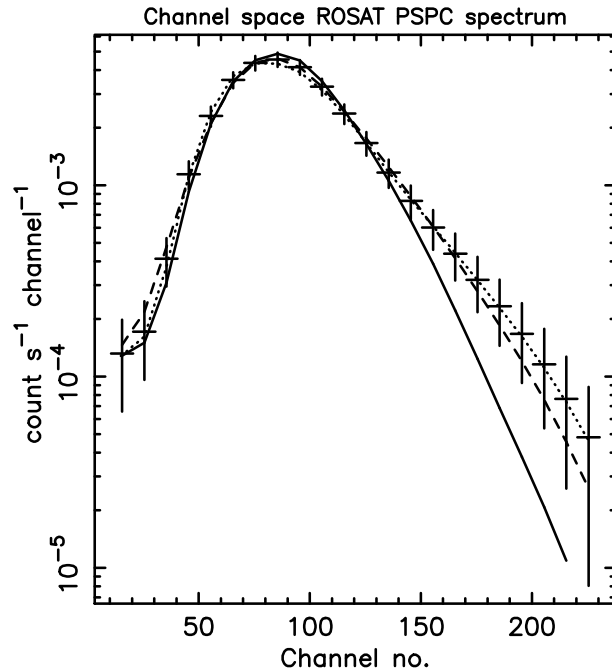


Figure 7. Channel space *ROSAT* PSPC spectrum of the bubble at $t = 15000$ yr shown with the three average best fit models (single temperature, abundance fixed at solar – solid line; single temperature, abundances fitted for – dashed; two temperature, abundances fixed – dotted) The two temperature and differential emission measure models give very similar *ROSAT* spectra. The spectrum has no noise, the error bars represent the size of typical Poisson uncertainties for an exposure time of 3000 s.

Table 4. Average result of fits to simulated *ROSAT* spectra using a single temperature MEKAL hot plasma model with absorption. The errors quoted are the deviations between the best fit results. See text for details. Note the significant improvement in fit when metal abundance is free to fit.

| Parameter | Single temperature fits | Units |
|------------------|-------------------------|---|
| N_{H} | 7.8 ± 0.4 | 10^{21} cm^{-2} |
| EM | 0.018 ± 0.005 | 10^{60} cm^{-3} |
| T | 0.163 ± 0.006 | keV |
| Z | 1.0 (Fixed) | Z_{\odot} |
| f_X (obs.) | 2.86 ± 0.07 | $10^{-12} \text{ erg s}^{-1} \text{ cm}^{-2}$ |
| f_X (int.) | 7.18 ± 1.84 | $10^{-10} \text{ erg s}^{-1} \text{ cm}^{-2}$ |
| χ^2 (d.o.f) | 39 ± 5.6 (19) | |
| N_{H} | 1.9 ± 0.4 | 10^{21} cm^{-2} |
| EM | 0.0019 ± 0.0012 | 10^{60} cm^{-3} |
| T | 0.45 ± 0.07 | keV |
| Z | 0.04 ± 0.02 | Z_{\odot} |
| f_X (obs.) | 3.29 ± 0.10 | $10^{-12} \text{ erg s}^{-1} \text{ cm}^{-2}$ |
| f_X (int.) | 0.17 ± 0.07 | $10^{-10} \text{ erg s}^{-1} \text{ cm}^{-2}$ |
| χ^2 (d.o.f) | 18.5 ± 4.8 (18) | |

after shell collapse the averaged temperature contributing to the photons detected by *ROSAT*, T_{ROSAT} , increases again. This is the emission from shocked wind itself, previously of too low a level compared to the X-ray emission from the shell to be noticeable.

Fig. 9 shows the best fit temperatures from single temperature fits to a set of simulated *ROSAT* spectra over time, for both metal abundance fixed at solar and abundances

Table 5. As Table 4 but fitting with a two temperature MEKAL model.

| Parameter | Two temperature fits | Units |
|------------------|-----------------------|---|
| N_{H} | 3.5 ± 2.8 | 10^{21} cm^{-2} |
| EM_1 | 0.04 ± 0.10 | 10^{60} cm^{-3} |
| T_1 | 0.23 ± 0.08 | keV |
| EM_2 | 0.00013 ± 0.00006 | 10^{60} cm^{-3} |
| T_2 | 1.28 ± 0.30 | keV |
| Z | 1.0 (Fixed) | Z_{\odot} |
| f_X (obs.) | 3.32 ± 0.10 | $10^{-12} \text{ erg s}^{-1} \text{ cm}^{-2}$ |
| f_X (int.) | 13.7 ± 32.9 | $10^{-10} \text{ erg s}^{-1} \text{ cm}^{-2}$ |
| χ^2 (d.o.f) | 12.0 ± 4.6 (17) | |
| N_{H} | 3.7 ± 2.9 | 10^{21} cm^{-2} |
| EM_1 | 0.013 ± 0.031 | 10^{60} cm^{-3} |
| T_1 | 0.24 ± 0.11 | keV |
| EM_2 | 0.00005 ± 0.00006 | 10^{60} cm^{-3} |
| T_2 | 1.45 ± 0.37 | keV |
| Z | 6.7 ± 5.0 | Z_{\odot} |
| f_X (obs.) | 3.31 ± 0.11 | $10^{-12} \text{ erg s}^{-1} \text{ cm}^{-2}$ |
| f_X (int.) | 33.3 ± 80.9 | $10^{-10} \text{ erg s}^{-1} \text{ cm}^{-2}$ |
| χ^2 (d.o.f) | 11.5 ± 4.1 (16) | |

free to fit. As generating 10 Poisson realisations for each of ~ 50 spectra, fitting and finally averaging the results would be prohibitively time consuming, we have fitted the spectra with no Poisson noise applied. Comparison of this with the more rigorous method used earlier shows that this gener-

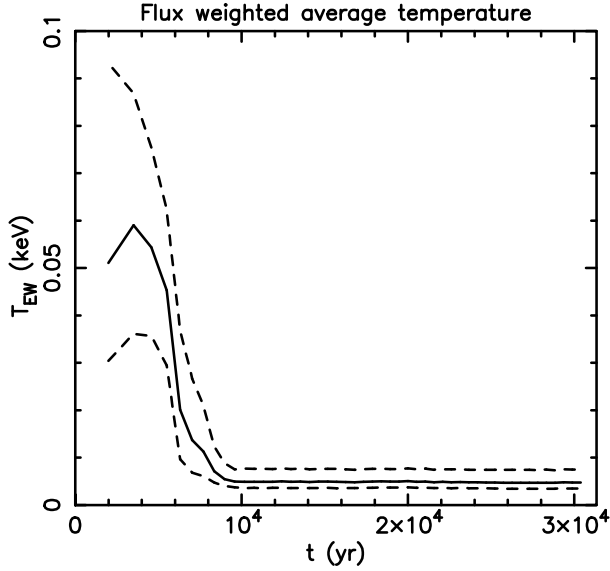


Figure 8. The flux weighted average temperature T_{EW} of the bubble (see Sect. 4.1), as a function of the age of the bubble, in the band 0.005–15.0 keV. At early times the emission is predominantly from the swept-up and shock heated ISM. After this shell cools the total bubble emission is still dominated by the shell, but the radiation is now UV rather than soft X-rays. Dashed lines show the r.m.s. deviation of T_{EW} .

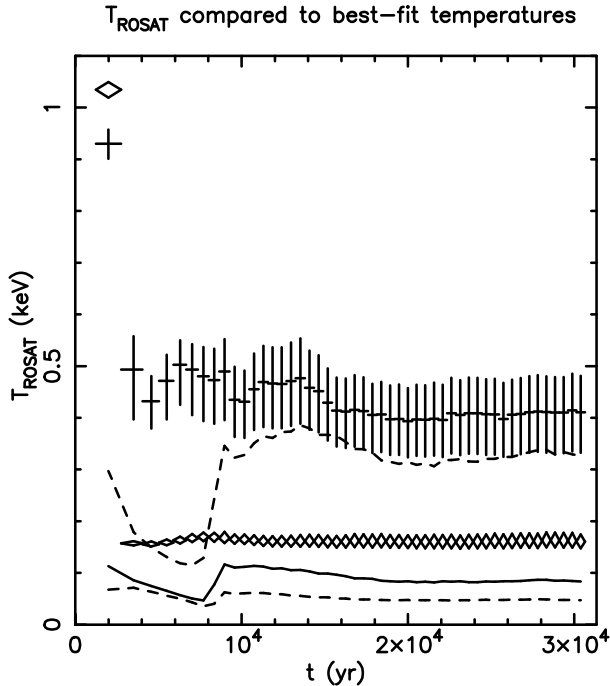


Figure 9. The *ROSAT* flux-weighted average temperature T_{ROSAT} as a function of bubble age (see Sect. 3.2.3), compared the temperatures obtained from single temperature fits to the PSPC spectra (Diamonds: fits with metal abundance fixed at solar, crosses: fits with metal abundance free to fit). Error bars are 68% confidence in one parameter of interest. The dashed lines show the r.m.s. deviation of T_{ROSAT} .

Table 6. As Table 4 but fitting with a differential emission measure model, where the emission measure at any temperature $EM(T) \propto T^\gamma$, between two cut-off temperatures T_{low} and T_{high} . This model attempts to recreate the multi-phase origin of the emission.

| Parameter | Diff. emission measure fits | Units |
|------------------|-----------------------------|---|
| N_H | 3.6 ± 2.3 | 10^{21} cm^{-2} |
| EM | 0.00376 ± 0.00524 | 10^{60} cm^{-3} |
| γ | -0.23 ± 0.36 | |
| T_{low} | 0.0118 ± 0.0345 | keV |
| T_{high} | 7.4 ± 2.2 | keV |
| Z | 1.0 (Fixed) | Z_\odot |
| f_X (obs.) | 3.37 ± 0.13 | $10^{-12} \text{ erg s}^{-1} \text{ cm}^{-2}$ |
| f_X (int.) | 1.46 ± 2.03 | $10^{-10} \text{ erg s}^{-1} \text{ cm}^{-2}$ |
| χ^2 (d.o.f) | 15.2 ± 6.3 (17) | |
| N_H | 3.0 ± 1.8 | 10^{21} cm^{-2} |
| EM | 0.00264 ± 0.00287 | 10^{60} cm^{-3} |
| γ | -0.29 ± 0.39 | |
| T_{low} | 0.0071 ± 0.0193 | keV |
| T_{high} | 8.7 ± 4.6 | keV |
| Z | 1.16 ± 1.53 | Z_\odot |
| f_X (obs.) | 3.38 ± 0.12 | $10^{-12} \text{ erg s}^{-1} \text{ cm}^{-2}$ |
| f_X (int.) | 0.81 ± 1.33 | $10^{-10} \text{ erg s}^{-1} \text{ cm}^{-2}$ |
| χ^2 (d.o.f) | 14.2 ± 5.7 (16) | |

ates essentially identical results, although the values of χ^2 obtained are misleadingly low.

As can be seen from Fig. 9 the best fit temperatures fail to reflect the temperature changes we know are occurring. Intriguingly, the best fit metallicity does show a systematic trend between $t \sim 5000$ and 10000 yr. Two temperature fits, able to fit the shape of the spectrum better, do show an initial drop in both temperatures to a minimum at $t \sim 5000$ yr, followed by an increase to a constant value after $t \sim 9000$ yr (although the hotter component only levels out after $t \sim 15000$ yr).

3.4 The high mass loss rate simulation

To further investigate how spectral fitting to the observed X-ray data depends on the the properties of the bubble, we have repeated the detailed analysis described in Section 3.2 on the higher wind mass loss rate simulation.

Increasing \dot{M}_W to $10^{-4} M_\odot \text{ yr}^{-1}$ results in a bubble with the same size at $t = 15000$ yr, identical cold shell properties, but a shocked wind with a density (temperature) a factor 2 higher (lower).

Single temperature models give best-fit results very similar to those given in Table 4 for the low mass loss rate simulation, except the best fit temperatures are significantly higher in this case: $T = 0.41 \pm 0.09$ keV (metal abundance fixed) or $T = 0.60 \pm 0.13$ keV (metal abundance fitted for). This is despite the average temperature within the shocked wind being half that of the low mass loss rate simulation. Again absorption columns (and when fitted for, metallicities) deviate systematically from the true values.

The two temperature spectral models give best fits very similar to the results given in Table 5, the best fit temperatures being $T_1 = 0.26 \pm 0.07$ keV and $T_2 = 1.47 \pm 0.31$ keV. The only real differences are a) the relative fraction of the total emission measure in the hot component has increased

(i.e. the spectrum appears to be harder), and b) there is evidence for two fit minima, one with low N_{H} and emission measure, the other a high N_{H} with high emission measure.

4 DISCUSSION

4.1 Properties inferred from the spectral fitting

We shall concentrate on the results from the low mass loss rate simulation, mentioning only where the spectral fit results from the high mass loss rate simulation differ.

4.1.1 Single temperature models

Single temperature spectral fits give misleading information on the state of the bubble, not surprising given the multi-component temperature structure and the detector characteristics, nor are they sensitive to the true spectral changes that occur during the bubble's growth (see Fig. 9). This suggests that the best-fit values are strongly affected by the multicomponent structure and the instrument response.

The confidence levels from the fits misrepresent the true uncertainties in the fitted parameters. In particular the fitted temperatures are apparently well constrained, although the emission comes from a very broad temperature distribution. The spectral fits give little clue to the true temperature distribution, as the fits with metallicity free to fit have acceptable χ^2 . A naive hope that in a situation such as this, with a broad, non-peaked temperature distribution, single temperature fits would show poorly constrained best-fit temperatures is not justified by these results.

Absorbing columns and metal abundances are both systematically mis-fitted. It is clear that by fitting a multicomponent spectrum with a single temperature model we introduce a major systematic effect. Single temperature fits with metal abundance fixed at solar (Table 4) are generally unacceptable, with reduced $\chi^2 \sim 2$, perhaps indicating that the model is not a good representation of the data. The hydrogen columns deviate significantly from the true absorbing column.

Freeing the metal abundance to fit does give good fits to the data, but at the expense of giving best-fit parameters that bear little relation to the bubble's true properties. The best fit metal abundances are less than one twentieth solar, and apparently strongly constrained. This is interesting given the current debate over the accuracy of X-ray determined abundances (*c.f.* Bauer & Bregman 1996).

The flux-weighted average temperature T_{ROSAT} derived in Section 3.2.3 is not a good estimator of the best-fit temperature, as can be seen in Fig. 9. An average temperature, even sensibly weighted, does not reflect how spectral fitting works, and will not give acceptable results.

4.1.2 Two temperature models

These (Table 5) give significantly better fits to the data than the single temperature models and are slightly better than the differential emission measure models. The absorbing columns fit closer to the true value. The fits are insensitive to the metallicity, and would not force us to believe

they are significantly different from solar, unlike the single temperature models.

That the best-fit temperatures in the two temperature model fits to the low and the high mass loss rate simulations are so similar, with only the relative normalisation of the two components varying, suggests the temperatures are determined more by the *ROSAT* PSPC's response than the true temperature distribution of the source.

4.1.3 Differential emission measure models

From Fig. 5 it is clear that for $T \lesssim 0.7$ keV the emission measure is well represented by a power law in T , with a slope of $\gamma \approx -1.8$. Between $T = 0.1$ keV and $T = 0.7$ keV the true emission measure falls by nearly two orders of magnitude, so a differential emission measure model with this slope should provide a good approximation to the spectrum.

The results of the model fits (Table 6) are therefore surprising, given the best fit values for $\gamma \approx -0.25$! The combination of material hotter than $T \sim 1$ keV and the energy dependent response of the *ROSAT* PSPC must bias the fit significantly. The slope is clearly wrong within the energy range 0.1-2.4 keV *ROSAT* is sensitive to, let alone extended to the cut-off temperatures claimed by the fit.

4.1.4 The effect of longer exposure times

Are any of the effects above due to low numbers of photons? Repeating the above analysis with assumed exposure times of 10000 s, giving simulated spectra with $\gtrsim 3000$ counts, gives results very similar to those in Section 3. The confidence regions quoted on the individual fits are smaller, but the average best fit result is consistent with those quoted above, and are statistically acceptable fits.

It therefore appears that the systematic deviations of the spectral fit results from the true values is due to fitting an intrinsically complex spectrum with a simplistic model, and not due to poor photon statistics.

4.1.5 Inferred properties

Can we infer any of the true bubble properties from the spectral fits? In particular, the true luminosity, densities, pressures and thermal energy are interesting quantities that we would like to know in addition to the temperature if X-ray observations are to be of any use in understanding the object.

The 0.1-2.4 keV fluxes predicted from all the models are reasonably accurate *before correction for absorption* (compare the real values from Table 2 with the results from the spectral fitting, Tables 4 - 6). The single temperature models get the intrinsic luminosity very wrong, due to the incorrect absorption column, either overestimating it by a factor ~ 5 (metallicity fixed at solar) or underestimating by an order of magnitude in the case of the fits with the metallicity free to fit. On average the two temperature models overestimate the intrinsic flux by an order of magnitude, although with a large uncertainty due to the large variation in best-fit column. Similarly the differential emission measure models also have a large scatter in inferred intrinsic luminosity.

Assuming we know the volume of the emitting plasma

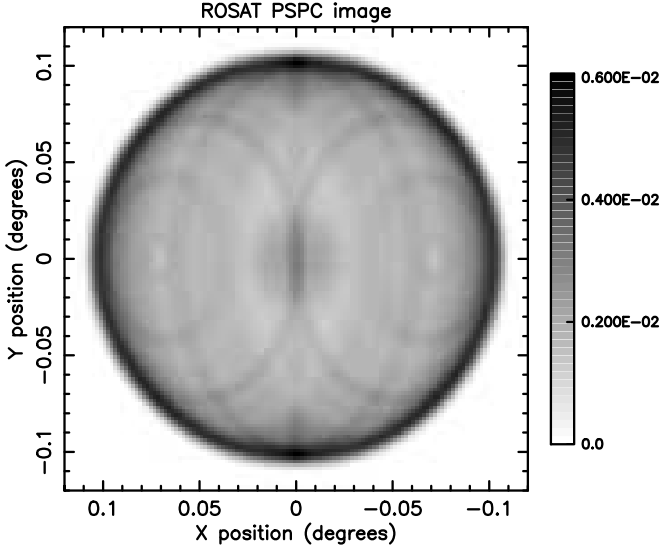


Figure 10. An X-ray image of the bubble at $t = 15000$ yr, in the 0.1-2.4 keV energy band. The image has been smoothed with a Gaussian of FWHM $25''$ to approximate the *ROSAT* PSPC PSF. Units are counts $\text{s}^{-1} \text{arcmin}^{-2}$.

V , the root mean square electron density is $n_e = \sqrt{(EM/V)}$, where EM is the (volume) emission measure obtained from the spectral fit. Then the thermal pressure and energy are $P \approx 2n_e kT$ and $E_{\text{TH}} \approx 3n_e kTV$.

Given the X-ray surface brightness (Fig. 10) we can estimate the volume. The inferred properties are relatively insensitive to V as P and n_e are proportional to $V^{-1/2}$ and $E_{\text{TH}} \propto V^{1/2}$.

The bubble is clearly limb-brightened (Fig. 10), the emission coming predominantly from a thin shell near the shocked-wind/cold shell interface. From a radial profile of the *ROSAT* surface brightness, and correcting for the point spread function, the inferred radial thickness of this shell is $\sim 20''$, the PSF-corrected volume $V_{\text{corr}} = 9.8 \times 10^{56} \text{ cm}^3$. By way of comparison, the total volume within the bubble inferred from the X-ray image is $V_{\text{bub}} = 6.0 \times 10^{57} \text{ cm}^3$. Note that this is less than the volume quoted in Table 2 as we are not including the cold shell.

The density, pressure and thermal energy inferred from the single temperature models, using V_{corr} and V_{bub} , are given in Table 7.

For the two temperature models, it would be sensible to associate the cool component (with a high emission measure) of the spectral fit, to cool, dense material near the shocked-wind/cold shell interface, given the observed limb brightening. The hot component in the fit, with a total emission measure two to three orders of magnitude less than the cool component, could well represent emission from the hot rarefied gas in the bubble interior. Assigning volumes V_{corr} and V_{bub} to the cool and hot components respectively we obtain densities, pressures and thermal energy content given in Table 7.

From the simulation we know the true properties of all the material in the bubble. The density in the plasma contributing the majority of the 0.1-2.4 keV flux (all the ma-

terial with volume emissivities within an order of magnitude of the maximum emissivity) varies between $2.5 \lesssim n_e \lesssim 28.2 \text{ cm}^{-3}$, averaging 7.8 cm^{-3} . In the hotter bubble interior the electron density is $n_e \approx 0.09 \text{ cm}^{-3}$. The shocked wind and cold shell are practically isobaric at $P = 1.3 \times 10^{-9} \text{ dyn cm}^{-2}$, and the majority of the total thermal energy in the bubble of $E_{\text{TH}} = 1.17 \times 10^{49} \text{ erg}$ is in the hot shocked wind material that occupies most of the bubble volume.

Comparing the inferred properties of the bubble from Table 7 with the true properties (see for example Fig. 4) we find:

- The single temperature spectral fits, assuming the emission come from a shell of volume V_{corr} , give, on average, estimates of the density and pressure (in the plasma that dominates the X-ray emission detected) that are within a factor 2 of the true values.
- Thermal energies inferred from single temperature models generally underestimate the true thermal energy in the bubble. The single temperature models are dominated by the cool gas, occupying only a fraction of the total volume, whose properties are not typical of the bubble as a whole, and miss the hotter gas that contains most of the thermal energy.
- Two temperature models give a better idea of the bubble properties, although the temperature of the hot component is significantly lower than the true temperature within the shocked wind.
- By attempting to fit a intrinsically multicomponent spectrum with simplistic single temperature model, the best fit hydrogen column and metal abundances can be significantly in error. In more complex models this effect is reduced, but not eradicated. For the three spectral models considered the fitted temperatures give little indication of the true temperature distribution.
- Spectral fits give a good estimate of the observed energy flux, but extrapolating the intrinsic source flux is error prone due to its strong dependence on the assumed absorption column, and may be an order of magnitude out.
- The results of the spectral fitting give little indication of the true variation in properties within the bubble, *i.e.* the multiple temperature components. In particular, components with temperatures outside the primary bandpass of the instrument are not represented by the spectral fitting. The differential emission measure model fails to give a better fit than a two temperature model, although on paper it should perform better. There would be little reason to believe that the two temperature model was in fact an over simplification of the true situation.
- The systematic error introduced by under-modeling the true spectrum will dominate over any statistical error on the best-fit parameters. The best fit may be a statistically good fit, but does not give any indication that it is a poor representation of the true properties.

It is interesting to note that despite the difference between the true bubble properties and those for a bubble with thermal conduction (compare the radial profiles in Fig. 4), the properties inferred from the *ROSAT* PSPC two temperature spectral fitting are generally consistent with a bubble with conduction:

- The predicted luminosity of a conductive bubble is

Table 7. Bubble properties as would be inferred from the *ROSAT* spectral fits to the low mass loss rate simulation. The volumes refer to the volumes defined in the text.

| Model | Volume | n_e (cm^{-3}) | P (dyn cm^{-2}) | E_{TH} (erg) |
|------------------------|-------------------|-------------------------------|---------------------------------|--------------------------|
| 1T, $Z = 1$ | V_{corr} | 4.3 | 2.2×10^{-9} | 3.3×10^{48} |
| | V_{bub} | 1.7 | 9.0×10^{-10} | 8.2×10^{48} |
| 1T, Z free | V_{corr} | 1.4 | 2.0×10^{-9} | 2.9×10^{48} |
| | V_{bub} | 0.6 | 8.0×10^{-10} | 7.3×10^{48} |
| 2T, $Z = 1$ (cool) | V_{corr} | 6.6 | 4.8×10^{-9} | 7.1×10^{48} |
| | V_{bub} | 0.15 | 6.1×10^{-10} | 5.5×10^{48} |
| 2T, Z free (cool) | V_{corr} | 3.1 | 2.9×10^{-9} | 4.3×10^{48} |
| | V_{bub} | 0.09 | 4.3×10^{-10} | 3.9×10^{48} |

slightly higher than that of the simulated bubble, but the spectral fits generally overestimate the intrinsic luminosity of the bubble.

- The temperatures predicted by the model with thermal conduction are $T \sim 1$ keV in the shocked wind, dropping to $T \sim 0.2$ keV in the denser material near the boundary with the cold shell (Fig. 4), very similar to the best fit temperatures.

- The mass flux off the cold shell driven by thermal conduction naturally leads to a region of warm X-ray emitting gas of the right density just inside the cold shell.

- Only the density of the hot component is inconsistent with the value predicted by the model with thermal conduction. The inferred density in the hotter material is too low by a factor ~ 5 .

4.1.6 High mass loss rate simulation

The true properties of the bubble in the high mass loss rate simulation are practically identical to those of the low mass loss rate bubble. The only differences are that the density and temperature in the shocked wind are a factor of two different. The intrinsic X-ray luminosity in the 0.1-2.4 keV band is 3% higher, but most importantly the *ROSAT* count rate is double that of the low mass rate simulation.

The intrinsic luminosity is again dominated by the cool, dense material near that shocked wind/cold shell interface, whose properties are almost identical between the two simulations.

The count rate depends on both the intrinsic spectrum and the detector’s spectral response. In this case the cooler bubble interior brings the emission from the shocked wind more within the *ROSAT* spectral response, giving more high energy photons in the PSPC spectra, and hence making them seem harder. This explains the higher best-fit temperatures of this cooler bubble, compared to the low mass loss rate simulation.

This is further evidence, if needed, that it is necessary to predict the *observable* properties of a model when comparing observation with theoretical models.

4.1.7 Summary of “observed” properties

Fitted absorption columns can vary wildly in a case with a complex spectrum, biasing estimated emission measures are luminosities. It might be safer not to fit for the column, and use estimates from optical or HI measurements.

The metallicity in single temperature models is badly underestimated. Given the current debate over X-ray determined abundances (Bauer & Bregman 1996), where much of the attention has concentrated on the hot plasma codes rather than the effect of multi-temperature gas, this is a very interesting result. Is this a peculiarity of this particular model, or a general property? Does this also affect higher spectral resolution instruments such as *ASCA* or the future *XMM*?

As single temperature fits fail to represent to true emitted spectrum they generally underestimate the thermal energy in the bubble, as this is primarily in hot, tenuous gas with much lower emissivity than the cool gas. We note that this could provide an explanation for the apparent discrepancy reported by Magnier et al. (1996) between the thermal energy in the superbubble N44 as derived from *ROSAT* and *ASCA* spectral fits, where the X-ray derived thermal energy is a factor 6-10 lower than expected on the basis of the Weaver et al. model. However, we have not demonstrated that our results apply over such a wide range of parameter space, and the alternative explanation that the stellar wind energy input may have been overestimated may well be true. We are continuing this work to specifically model superbubbles in future papers.

Nevertheless, it is safe to say that the results of simple spectral fits to what are in reality more complex sources depend strongly on both the spectral response of the detector and the spectral distribution of the source.

4.2 Limitations and assumptions

We have not included several physical effects that are potentially important in real stellar wind blown bubbles: thermal conduction, magnetic fields, time-dependent ionisation, non-solar abundance ratios, mass loading and interaction with the winds from the main sequence and red giant stages of the star. Mass and energy were injected onto the computational grid in a manner more suitable for superbubbles around OB associations and in starburst galaxies. For the spectral fitting, we have ignored the soft X-ray background.

These omissions do not invalidate or reduce the significance of the results contained in this paper. Our aim is to illustrate the need for modeling the X-ray emission, and analysing in as similar a manner to real observations as possible. In this introductory paper we have avoided the potential complications that additional physics would introduce into the interpretation of the results, and take the known properties from relatively simple model, calculate what would be seen in a real observatory such as *ROSAT*, and ask “can we infer the true properties from the X-ray emission resulting from those properties?” Relaxing the above assumptions only make the need for this method of direct comparison more urgent.

4.3 Future work

We intend to extend this work, relaxing the assumptions of constant mass and energy injection, and a homogeneous ISM, to model the properties of superbubbles and galactic winds in starburst galaxies. As a general method and philosophy it can, of course, be applied to a wider range of astrophysical bubbles.

In future we shall consider the spatial variation of the X-ray properties, as done for example for the *ROSAT* observation of M82's galactic wind by Strickland, Ponman & Stevens (1997).

We shall also extend this work to other X-ray observatories such as *ASCA* or *XMM*, to make use of the superior spectral resolution of these instruments. For the higher signal-to-noise spectra that *XMM* will make available, this method of direct comparison will be absolutely necessary!

5 CONCLUSIONS

We have shown that in order to compare X-ray observations to theory, it is necessary to consider the *observable* X-ray properties of the theory. The results of a spectral fit are a complex function of the the density and temperature distributions of the source, absorption, the properties of the detector used and the spectral fitting procedure. As such they should not be considered as “real” values, but as characteristic values, and specific to the instrument used. The normal method of fitting a simplistic model to the observed data, and then treating the best-fit parameters as the real properties can easily give answers an order of magnitude out from the truth.

This technique will allow the first direct comparison between observation and theoretical models of superbubbles and starburst driven outflows.

We would like to thank Trevor Ponman, Robin Williams and the referee for constructive criticism. DKS and IRS acknowledge financial support from PPARC. This work was performed on the Birmingham node of the STARLINK network.

REFERENCES

- Arnaud K., Borkowski K. J., Harrington J. P., 1996, *ApJ*, 462, L75
- Band D. L., Liang E. P., 1988, *ApJ*, 334, 266
- Bauer F., Bregman J. N., 1996, *ApJ*, 457, 382
- Belloni T., Mereghetti S., 1994, *A&A*, 286, 935
- Blondin J. M., Kallman T. R., Fryxell B. A., Taam R. E., 1990, *ApJ*, 356, 591
- Briel U. G. et al., 1994, *The ROSAT user's handbook*. Max-Planck-Institut Für Extraterrestrische Physik, München
- Castor J., McCray R., Weaver R., 1975, *ApJ*, 200, L107
- Chevalier R. A., Clegg A. W., 1985, *Nature*, 317, 44
- Colella P., Woodward P. R., 1984, *J. Comput. Phys*, 54, 174
- Corcoran M. F., Rawley G. L., Swank J. H., Petre R., 1995, *ApJ*, 445, L121
- García-Segura G., Mac Low M.-M., Langer N., 1996, *A&A*, 305, 229
- Hartquist T. W., Dyson J. E., Pettini M., Smith L. J., 1986, *MNRAS*, 221, 715
- Heckman T. M., Armus L., Miley G. K., 1987, *AJ*, 93, 276
- Kreysing H. C., Diesch C., Zweigle J., Staubert R., Grewing M., Hasinger G., 1992, *A&A*, 264, 623
- Leahy D. A., Zhang C. Y., Kwok S., 1994, *ApJ*, 422, 205
- Leahy D. A., Zhang C. Y., Volk K., Kwok S., 1996, *ApJ*, 466, 352
- Mac Low M. M., McCray R., Norman M. L., 1989, *ApJ*, 337, 141
- Magnier E. A., Chu Y. H., Points S. D., Hwang U., Smith R. C., 1996, *ApJ*, 464, 829
- Masai K., 1994, *ApJ*, 437, 770
- Mellema G., Frank A., 1995, *MNRAS*, 273, 401
- Mewe R., Kaastra J. S., Liedahl D. A., 1995, *Legacy*, 6, 16
- Morrison R., McCammon D., 1983, *ApJ*, 270, 119
- Raymond J. C., Smith B. W., 1977, *ApJS*, 35, 419
- Soker N., 1994, *AJ*, 107, 276
- Spitzer L., Jr. 1962, *Physics of Fully Ionized Gases*. Interscience, New York
- Stevens I. R., Blondin J. M., Pollock A. M. T., 1992, *ApJ*, 386, 265
- Strickland D. K., Ponman T. J., Stevens I. R., 1997, *A&A*, 320, 378
- Vishniac E. T., 1983, *ApJ*, 274, 152
- Volk H., Kwok S., 1985, *A&A*, 153, 79
- Watson M. G., Stanger V., Griffiths R. E., 1984, *ApJ*, 286, 144
- Weaver R., McCray R., Castor J., Shapiro P., Moore R., 1977, *ApJ*, 218, 377
- Wrigge M., Wendker H. J., Wisotski L., 1994, *A&A*, 286, 219
- Zhekov S. A., Perinotto M., 1996, *A&A*, 309, 648